ROYAL SOCIETY
OF CHEMISTRY

PAPER

Check for updates

Carbonate-hosted sphalerite weathering regulates cadmium mobilization in soils

Xin-yang Li, [*ab] Juan Liu,[a] Peng-jie Hu,[a] Jia-wen Zhou,[a] Yong-ming Luo,[a] Long-hua Wu*[a] and Michael Schindler [b]

Cadmium (Cd)-bearing sphalerite occurs in carbonate-hosted zinc (Zn) deposits and can be deposited as particulate matter (PM) on the surrounding soils during mining activities. Weathering of the sphalerite-bearing PM releases Cd, yet the role of associated carbonates in controlling Cd mobility remains unclear. This study investigates Cd mobilization from carbonate-hosted sphalerite ore particles (SP) and Cd distribution between solid and aqueous phases in acidic and alkaline soils. At low Ca/S ratios, sphalerite dissolution led to similar annual Cd mobilization rates in acidic (1.41 µg Cd per g SP per a) and alkaline soils (1.29 µg Cd per g SP per a). However, higher Ca/S ratios significantly reduced Cd mobility due to Cd retention as $CdCO_3$ in both solid and solution phases. In acidic soils, Cd-bearing sphalerite weathering caused Cd depletion and enrichment in sulfide ore and $CaCO_3$ phases, respectively. In alkaline soils, $CdCO_3$ nanomaterials precipitated on zincite due to the incompatibility of Cd with the structure of ZnO and its desorption from the negatively charged Fe (hydr)oxide surfaces. For all characterized samples, nanoparticulate (nano)-Cd showed significant positive correlations with nano-Fe and nano-organic carbon (bulk chemical data) and was sequestrated as $CdCO_3$ nanomaterial by OM-Fe (hydr)oxide colloids in soil solutions (TEM data). These observations highlight that Cd-bearing nanomaterials control Cd mobilization in carbonate-rich soils affected by sphalerite-bearing PM deposition.

Environmental significance

Cadmium (Cd) contamination from the weathering of carbonate-hosted sphalerite poses long-term environmental risks in mining-impacted soils. This study reveals that the formation and transformation of Cd-bearing nanoparticles and colloids regulate Cd mobility in both acidic and alkaline soils, where traditional bulk chemistry fails to fully capture its environmental fate. Cd interacts with carbonates, Fe(hydr)oxides, and organic matter to form stable or mobile nano-materials, which control Cd mobility into soil solutions. These nanophases differ between acidic and alkaline soils, underscoring the critical role of interfacial processes in Cd transport. The findings provide critical insight into Cd behavior in carbonate-rich environments and the need to integrate nanoscale miner-alogical dynamics into risk assessment and remediation strategies for carbonate-rich Cd-contaminated soils.

1. Introduction

Cadmium (Cd) contamination in soils poses significant environmental and health risks due to its high toxicity and persistence. Sphalerite is one of the primary geological sources of Cd.[1] The dissolution of sphalerite leads to Cd release and enrichment in the surrounding soils.[2] The proposed mechanism of sphalerite dissolution includes acid-promoting dissolution (APM) ((Zn, Cd)S + 2H$^+$ → Zn^{2+}/Cd^{2+} + H$_2$S) and oxidation-promoting dissolution (OPM) (S^{2-} → SO$_4$$^{2-}$, Zn^{2+}/Cd^{2+} release).[3,4] Several studies reported a dynamic release of Cd during the dissolution of sphalerite. However, there is still a lack of knowledge about how the dissolution of Zn sulfide ore affects Cd mobility in soils as the former ore is a mineralogical complex system containing various host rocks and associated wall rocks (*e.g.*, carbonate rocks).[5] Carbonate-hosted sphalerite weathering has been identified as a critical source of Cd in soils around mining areas worldwide, *e.g.*, the Irish Midlands and Alpine regions in Europe,[5] the Tri-State and Upper Mississippi Valley in North America,[6] and the Andes of South America.[7]

The weathering of Zn sulfide ore in soils affects the redistribution of Cd and Zn on the surface of Zn ores and the Cd and Zn species in the colloidal fractions.[2,8] Abiotic and biotic-driven Ca–Me (Me = Zn, Cd) carbonate coatings on sulfide mineral surfaces have been shown to inhibit further sulfide dissolution and Cd release.[8,9] These processes are commonly at the nano-meter scale and form either natural or incidental nanoparticles (NPs) in soils. For example, CdS and CdCO$_3$ nanoparticles (NPs) can be respectively formed during dissolution–reprecipitation processes involving Cd-bearing sphalerite and Cd-bearing

State Key Laboratory of Soil and Sustainable Agriculture, Institute of Soil Science, Chinese Academy of Sciences, Nanjing 211135, China. E-mail: lhwu@issas.ac.cn; Xinyang.Li@umanitoba.ca

Department of Earth Sciences, University of Manitoba, Winnipeg, Manitoba R3T 2N2, Canada

3652 | *Environ. Sci.: Processes Impacts*, 2025, **27**, 3652–3664

This journal is © The Royal Society of Chemistry 2025

calcite,[10–14] which are driven by the formation of porosity along multiphase interfaces.[15] Cd is generally incorporated into sulfide (*e.g.*, sphalerite) and carbonate (*e.g.*, smithsonite and calcite) due to the isomorphic substitution of Zn by Cd in ZnS and $ZnCO_3$ and Zn-bearing $CaCO_3$, which favors Cd sequestration even in acidic soils.[16,17] However, Cd^{2+} may exhibit limited substitution into some metal oxides, such as zincite (ZnO), due to the crystal-chemical incompatibility of Cd with the ZnO structure,[18,19] resulting in the higher potential mobilization of Cd relative to Zn ores. However, there is still a lack of microscopic evidence of how Cd mobility is controlled by interfacial dissolution precipitation processes involving different phases within carbonate-hosted sphalerite in soils.

Colloids are important carriers of metal contaminants in mining-impacted soil environments. In contrast to sphalerite, the dissolution of carbonate-hosted sphalerite would release significant quantities of Ca^{2+} into the soil system, which promotes the compression of a diffuse double layer on mineral and colloid surfaces, flocculation and subsequent colloid aggregation.[20] High content of Ca^{2+} drives the structural transition of metal-bearing organic matter (OM) from a colloidal state to a micrometric Ca-branched OM,[21,22] which alters the metal redistribution and mobility in colloids. These Ca-mediated colloidal transitions may either immobilize Cd *via* aggregation[8] or enhance its dispersal if stable Cd-bearing colloids form (*e.g.*, crystalline CdS and $CdCO_3$).[23] However, traditional bulk soil chemical analyses or dissolved-phase measurements cannot capture these nanoscale processes, significantly underestimating Cd mobility.[24] Cd-bearing nanomaterials, including precipitates, nanoparticles, and colloids, can act as cryptic vectors for Cd transport, bypassing predictions based solely on bulk soil chemistry or dissolved ion concentrations.[25] This gap is particularly acute in carbonate-rich mine soils, where high pH and Ca^{2+} levels create unique conditions for colloidal interactions. Despite the importance of colloids in controlling metal mobility, the relationship between Cd-bearing colloids in soil solutions and Cd-sphalerite weathering in bulk soils remains poorly understood. Therefore, complex interactions between Cd-bearing sphalerite with soil constituents and the potential formation of Cd-bearing nanomaterials (precipitates, colloids and nanoparticles) need to be considered when evaluating the mobility of Cd in soils around carbonate-hosted Pb–Zn mine areas. Furthermore, quantification of the release of Cd during the interaction of carbonates with sphalerite and soil constituents will guide remediation strategies for Cd-contaminated soils in Zn mining areas worldwide.

Accordingly, the objectives of this study are to (1) quantitatively determine the dissolution of SP at different Ca/S ratios spiked in acidic and alkaline soils at the bulk scale; and (2) characterize the footprint of Cd-bearing phases in colloids from soil solutions and mineral grains at the nano- to microscale using a combination of the focused ion beam (FIB)-scanning electron microscope (SEM) and transmission electron microscope (TEM). We hypothesize that interfacial dissolution precipitation processes involving different phases within carbonate-hosted sphalerite will control the transition of Cd from soils to soil solutions. Hence, the results of this study allow future studies to model and predict the mobility and bioavailability of heavy metals in soils impacted by mining activities of carbonate-hosted Pb–Zn deposits.

2. Materials and methods

2.1 Soil and ore sampling, preparation

Acidic sandy loam and alkaline silt loam from unpolluted farmland soils were sampled in Yunlong and Huidong counties in Southwestern China. The soil samples were air-dried, crushed, and sieved with 2 mm and 0.15 mm meshes. The 2-mm sieved soils were used to determine physicochemical properties (pH, soil organic matter (SOM), effective cation exchange capacity (eCEC) and soil texture) and the 0.15-mm sieved soils were selected for metal analyses (SI). The soils differed in terms of their OM content and chemical composition. The acidic soils (2.5%) have a higher OM content than the alkaline soils (1.3%). Total S of the former (347 mg kg^{-1}) was also higher than in the latter (73 mg kg^{-1}), whereas the concentrations of total Ca and Fe were higher in the alkaline (22.3% and 6.7%) than in acidic soils (0.6% and 2.1%) (Table S1).

Three Zn-ore samples (SP1, SP2, and SP3) used in this study were collected from the Jinding and Daliangzi Pb–Zn deposits in Southwestern China, using a Teflon shovel to prevent unintentional metal contamination. After cleaning, the ore samples were ground to particles with a diameter smaller than 63 μm (representing clay- and silt-size particles, which were thought to account for most of the fugitive dust mass flux[26]). Chemical and mineralogical analyses were conducted using inductively coupled plasma-optical emission spectrometry (ICP-OES, Avio 200, PerkinElmer) and powder X-ray diffraction (XRD) (SI). The Ca/S ratio in SPs increases in the sequence SP1 < SP2 < SP3 (Table S2), which is in line with the change in ratios between the major diffraction peaks for calcite and sphalerite in the XRD pattern (Fig. S1). At the micrometer scale, more than 30 areas were analyzed using SEM-EDS and an electron microprobe (EPMA) to determine the Cd concentrations in various minerals of SP-ores. These analyses indicated that most Cd occurred in sphalerite grains and minimal amounts in the $ZnSO_4$ and $ZnCO_3$ phases (Fig. S2).

2.2 Soil incubations and leaching experiment

Batch incubations (≤12 months) were conducted in polypropylene beakers using 100 g aliquots of the experimental soils. The 12-month incubation period was chosen to capture both fast and slower processes.[27] Ionic Cd ages quickly, usually within ~60 days. Longer times are needed for secondary carbonate precipitation and colloid changes. A one-year incubation period, therefore, provided a good balance between practical duration and chemical processes. The soils were spiked with or without ground sphalerite ores (SP) (1.000 ± 0.005 g) in four treatments (control: without Zn ore-spiking; SP1: with SP1-spiking; SP2: with SP2-spiking; SP3: with SP3-spiking). This amount corresponds to deposition fluxes of

This journal is © The Royal Society of Chemistry 2025

Environ. Sci.: Processes Impacts, 2025, **27**, 3652–3664 | **3653**

2.35 and 34.2 mg per m^2 per year, which fall within reported Cd deposition ranges of mining dust (0.11 to 57.7 mg per m^2 per year),[28,29] ensuring environmentally realistic simulation of farmland conditions. It is noteworthy that the soil bulk density (1.3 g cm^{-3}) and soil depth (30 cm) simulate typical farmland soil.[30] To ensure a continuous 65% field water capacity, the water content was regulated by weighing the incubations and compensating for lost mass by supplementing Milli-Q water. This water content resulted in an unintermittent oxygen–water interface, as indicated by changes in Eh values during one water replenishment cycle (Fig. S3).

Soils were collected on days 0, 30, 90, 180, and 365 for freeze-drying and analyzed for soil pH and total Cd, as well as Cd extractable with CaCl$_2$ and EDTA (Table S5). The concentrations of SO$_4{}^{2-}$ and CO$_3{}^{2-}$ in the CaCl$_2$-extracts were determined by ion chromatography (IC, Thermo Fisher). Zn-bearing grains in the SP2-spiked acidic and alkaline soils were characterized with SEM-EDS, and two regions of interest depicting sphalerite-CaCO$_3$ and Zn oxide-Fe (hydr)oxide interfaces were extracted with FIB and prepared for subsequent TEM studies. These interfaces represent the dominant reactive microsites controlling Cd mobility from Cd-bearing Zn minerals to soils.

Column leaching experiments were conducted to determine the chemical compositions of the dissolved and colloidal fractions of the soils and to identify the type of colloid with TEM. These macroscopic to nanoscopic studies helped to determine any temporal changes in the concentrations and speciation of Cd and other elements in both fractions throughout the experiments (i.e., after 0, 90, 180 and 365 days).

After filtration and ultrafiltration, the leachates were analyzed for the truly dissolved and nanoparticulate fractions of Cd, Zn, Fe and DOC using inductively coupled plasma mass spectrometry (ICP-MS) and IC. Part of the leachates in the acidic soil were also used for ultracentrifugation to separate the colloid fractions from the supernatants for subsequent TEM analysis. Details of incubation and leaching experiments and chemical analysis of Cd in soils are listed in Sections 3–4 of the SI.

2.3 Cd mobilization rate in SP-spiked soils

In our study, the weathering of SP ores resulted in the mobilization of Cd. A mobilization rate (MR) was used to determine the Cd release capacity from metal-bearing sphalerite ore (eqn (1)).

$$\mathrm{MR}_i \, (\%) = (M_{i\text{-CaCl}_2/\text{EDTA}} - M_{0\text{-CaCl}_2/\text{EDTA}})/M_{i\text{-total}} \times 100\% \quad (1)$$

where M_i and M_0 indicate the concentration of Cd in SP-spiked soil at different incubation times and at day-0; CaCl$_2$/EDTA and Total represent the CaCl$_2$- or EDTA-extractable and total concentration of Cd.

2.4 Relative contribution of APM and OPM

This study only determined APM for the acidic soils as APM was buffered in the alkaline soils. In acidic soils, APM and OPM processes operate simultaneously but at different intensities depending on soil conditions. To quantify their contributions, we combined Cd mobilization with changes in proton activity

(i.e., soil pH) and carbonate content. ZnS and carbonates control APM and S^{2-} (of ZnS) and the background soil control the OPM process. Here, the temporal changes of carbonate and pH were used to determine OPM through integrating the real-time pH and proton consumption by carbonate (as otherwise the potential proton release induced by S^{2-} (of ZnS) oxidation would be reckoned). Then, APM was calculated by subtracting mobilized Cd released by OPM from the total mobilized Cd (eqn (2)–(5)). The relative contribution (%) of [OPM] and [APM] at each incubation time was calculated.

$$[\mathrm{OPM}]_i = \{((\Delta[\mathrm{H}^+]_{\mathrm{molar1}}) + (\Delta[\mathrm{H}^+]_{\mathrm{molar2}})) \times [\mathrm{Cd}]_{\mathrm{molar}}\}_i \quad (2)$$

$$[\mathrm{APM}]_i = \Delta[\mathrm{Cd}]_{\mathrm{EDTA}\text{-}i} \times W_{\mathrm{soil}} - [\mathrm{OPM}]_i \quad (3)$$

$$\Delta[\mathrm{H}^+]_{\mathrm{molar1}} = 10^{-\Delta \mathrm{pH}_i} \times 0.25 \quad (4)$$

$$\Delta[\mathrm{H}^+]_{\mathrm{molar2}} = \frac{\Delta\left[\mathrm{CO}_3{}^{2-}\right]_i \times W_{\mathrm{soil}}}{\left[\mathrm{CO}_3{}^{2-}\right]_{\mathrm{molar}}} \quad (5)$$

where i indicates the incubation time, [OPM] and [APM] the amount of mobilized Cd released via OPM and APM (Table S4), $\Delta[\mathrm{H}^+]_{\mathrm{molar1}}$ and $\Delta[\mathrm{H}^+]_{\mathrm{molar2}}$ the molar number induced by carbonate consumption and the real-time molar number at each incubation time; [Cd]$_{\mathrm{molar}}$ is the molar concentration of Cd (114.2 g mol^{-1}), $\Delta[\mathrm{Cd}]_{\mathrm{EDTA}}$ is the increased EDTA-extractable Cd (mg kg^{-1}) relative to day 0, W_{soil} is the soil weight in our incubations, $\Delta[\mathrm{CO}_3{}^{2-}]$ indicates the decrease in the amount of carbonate (mg kg^{-1}) relative to day 0; $\Delta[\mathrm{pH}]$ indicates the change in pH relative to day 0, the parameter 0.25 represents the coefficient of water holding content and [CO$_3{}^{2-}$]$_{\mathrm{molar}}$ is the molar concentration of CO$_3{}^{2-}$ (60 g mol^{-1}).

2.5 FIB-SEM-TEM characterization of selected interfaces

SEM was used to characterize the samples (365-day) at the micrometer scale and to identify interfaces between Zn-bearing phases for subsequent examinations at the nanometer scale. Circa 100 mg of the acidic and alkaline soils were embedded in epoxy resin molds with a 1 : 5 ratio of hardener–resin mixture under constant stirring. The molds were cured for 48 h at room temperature and then polished with Micro-Polish alumina powder on 8-inch Nylon PSA Buehler discs. The carbon-coated epoxy pucks were then analyzed using an environmental field-emission scanning electron microscope (FEI Quanta 650 FEG Environmental SEM) under an accelerating voltage of 20 kV and a beam current of 1 nA. Hotspots of interactions between sphalerite-CaCO$_3$ and Fe (hydr)oxide-Zn minerals were subsequently selected for FIB extraction (Zeiss Crossbeam 550).

After FIB extraction, TEM investigations were performed with an FEI Talos 200x and Tecnai G2 F20 S-Twin at 200 KV. High-angle annular dark-field (HAADF) imaging and energy dispersive spectroscopy (EDS) were conducted in STEM mode and selected area electron diffraction (SAED) in TEM mode.

2.6 Analysis of the colloids from the leaching experiment

In this study, the dissolved and truly dissolved fractions are defined as the constituents in filtrates after filtration (0.45 µm

3654 | Environ. Sci.: Processes Impacts, 2025, 27, 3652–3664

This journal is © The Royal Society of Chemistry 2025

filters) and ultrafiltration (10 kDa filter).[8] The differences between 10 kDa–0.45 μm and <10 kDa were defined as nanoparticulate and truly dissolved fractions, respectively.

The leachates collected on day 0, 90, 180, and 365 in both acidic and alkaline soils were ultrafiltered. The leachates collected from the column experiments were filtered through 0.45-μm pore-size PES disposable filters (Membrana GmbH, Wuppertal, Germany), and each filtrate was divided into two aliquots. One was for the DOC and elemental (*e.g.*, Cd and Fe) analyses using a TOC-Analyzer (Shimadzu, Japan) and ICP-MS and ICP-OES. The other aliquot (A1) was filtered through an Amicon Ultra-15 centrifugal filter unit. After centrifugation for 30 min at $4000 \times g$, part of the filtrate was used to measure DOC and the concentrations of truly dissolved metals (A2) using ICP-MS. The Cd, Fe and DOC proportions in the nanoparticulate (10 kDa–0.45 μm) fractions were calculated by subtracting the respective concentrations in A2 from A1.

TEM studies were conducted on colloids extracted from soil leachates at days 0, 180, and 365 during incubations of SP2-spiked treatments. At each time, the leachate was centrifuged at 171 500 g for 90 minutes using ultracentrifugation (Optima MAX-UP, Beckman Coulter, USA). Several microliters were extracted with a syringe and placed on copper grids (400-mesh). The liquids remained on the grid for about 10 seconds and were then removed with a paper wipe. This procedure was repeated three times. The deposited colloids were subsequently examined using TEM to determine their morphology and composition. Metal-bearing phases in the colloids were identified using a combination of *d*-spacings observed in selected area electron diffraction (SAED) patterns, high-resolution TEM (HRTEM) images, and semi-quantitative chemical analyses determined with EDS in scanning TEM mode. More than 20 colloids were analyzed to ensure statistical accuracy.

3. Results and discussion

3.1 Temporal changes of pH, sulfate and carbonate activities in carbonate-rich SP-spiked soils

Higher pH occurs in SP-spiked acidic soils with a high Ca/S ratio, most likely due to the higher abundance of carbonates in these soils (Fig. S4a). Due to the high background concentrations of Ca in the alkaline soils, there is no difference in soil pH among the three SPs with different Ca/S molar ratios. Generally, the pH decreases in all SP-spiked soils from day 0 to day 365, except for a pH increase in SP1-spiked soil before day 90. After one year of incubation, the pH decreases by 0.19–0.41 units in the acidic soil and 0.45–0.71 units in the alkaline soil (Fig. S5).

The decline in soil pH results from the acid-producing abiotic and biotic oxidative dissolution of ZnS to aqueous Zn^{2+} and sulfate. This is in accord with an increase in SO_4^{2-} concentration in both acidic and alkaline soils with the ongoing dissolution of the SP. After one year of incubation, the SO_4^{2-} concentrations increase by 67.4–118.6 mg kg^{-1} in the acidic and 92.9–158.1 mg kg^{-1} in the alkaline soils. Though the SO_4^{2-} concentration increase is more significant in the alkaline than in the acidic soils, the rates in SO_4^{2-} production are similar in

both soils. The significant negative ($p < 0.05$, r^2 ranges from 0.942 to 0.974) linear relationships between the increase in SO_4^{2-} concentration and soil pH (Fig. S6) illustrate this process. As the oxidation process *via* atmospheric O_2 formally does not consume or release protons, the acidification is most likely caused by hydrolysis induced by Zn^{2+} ($Zn^{2+} + H_2O = Zn(OH)^+ + H^+$), proton release upon Zn^{2+} adsorption to soil minerals and OM[31] or the oxidation of sphalerite by Fe^{3+} ($ZnS + 8Fe^{3+} + 4H_2O \rightarrow Zn^{2+} + 8Fe^{2+} + SO_4^{2-} + 8H^+$). The latter oxidation occurs more frequently in acidic soils and less in alkaline soils due to the higher mobility of Fe^{3+} under acidic conditions. The competition effect between Ca^{2+} and H^+, *e.g.*, the Ca–O bond weakened by H^+,[32] could also render the desorption of surface-bound protons from minerals of high PZC (point of zero charges), such as goethite and gibbsite (PZC = 8–10), into soil solutions.

The correlation analysis (Table S3) indicates that the Ca/S ratio in the SP ore negatively correlates with pH (*i.e.*, there is a lower Ca/S ratio in the acidic than alkaline soils). Furthermore, the slight decrease in soil pH with incubation time under acidic conditions (Fig. S4a) indicates that the H^+ consumption by carbonate rocks in SPs outweighs the simultaneous H^+ release through SP dissolution. This buffering effect lasted 90 days in SP1-spiked soils and is more pronounced when the pH is equal to the pKa values for carbonic acid ($pK_{a1} = 6.35$ and $pK_{a2} = 10.33$) and thus less effective for pH values in between the pKa values. This would explain why a more significant decrease in pH occurs in the alkaline soils (pH 8–9) than in the acidic soils (pH 5.5–6.5).

The observed declines in pH (maximum of 0.41 and 0.71 units in acidic and alkaline soils) are, however, lower than those in soils spiked with pure sphalerite (maximum of 1.05 units),[33] indicating that ZnS more readily produces acid than the SP. This could be related to the S content, acidic buffering effect of mineral impurities ($CaCO_3$, PbS, CdS and SiO_2 shown by the XRD data in Fig. S1) in the SPs and the higher proportion of accessible surface areas for ZnS relative to the SP. For example, SP often contains coarser-grained ZnS embedded in a matrix of less reactive minerals (*e.g.*, carbonates, silicates), which reduces exposure to O_2 and water and thus limits dissolution rates.[34] Additionally, SP typically contains a lower S content and a higher number of different S species (*e.g.*, a mixture of sulfide and sulfate) than sphalerite alone,[27] which results in a lower acid production capacity relative to the latter mineral.

Furthermore, the proton consumption by carbonates in SPs may not reach a balance point to offset the acidification through oxidative ZnS dissolution during incubation, as reflected by the continuous decrease in pH throughout the experiment (Fig. S4a). However, a decreasing slope of the change in pH indicates that more protons are being buffered over time, most likely due to the increasing amount of dissolved carbonate species in the soil (Fig. S4b). The increase in the CO_3^{2-} concentration over time differs between the SP-treatments in the order: SP1 (average, 33.0 μg kg^{-1}) > SP2 (average, 17.7 μg kg^{-1}) > SP3 (average, 11.4 μg kg^{-1}). Thus, continuous proton consumption by carbonates in carbonate-rich SP, along with a decreasing number of reactive surface sites with increasing incubation time, most likely results in a reduction of H^+ release

This journal is © The Royal Society of Chemistry 2025

Environ. Sci.: Processes Impacts, 2025, **27**, 3652–3664 | **3655**

and, consequently, a decrease in the mobility and bioavailability of heavy metals released by the SP.

These results suggest that monitoring pH and the amount of dissolved carbonate species is a powerful tool to monitor the potential release of heavy metals during the weathering of ore particles deposited on soils by aeolian processes.

3.2 Extractable Cd in SP-spiked soils

Irrespective of the types of SPs, the amounts of mobilized-Cd calculated from $CaCl_2$- and EDTA-extractable Cd increased with the incubation time, indicating ongoing oxidative dissolution of sphalerite and Cd release over the incubation time (Fig. S7). For $CaCl_2$–Cd, the mobilized-Cd in the acidic soils (average, 0.11 mg kg^{-1}) is 2–3 orders higher than in the alkaline soils (Fig. S7a and b). For EDTA-Cd (Fig. S7c and d), the mobilized-Cd in the acidic soils (average, 0.58 mg kg^{-1}) is similar to that for the alkaline soils (average, 0.61 mg kg^{-1}). Irrespective of the soils, the mobilized-Cd in the different SP-spiked treatments increases in the sequence SP1 < SP2 < SP3, except for the $CaCl_2$–Cd obtained from the alkaline soils. This ranking is inversely correlated with the Ca/S ratio, which decreases in the sequence SP1 > SP2 > SP3. These results suggest that higher $CaCO_3$/sulfide ratios in the SP inhibit Cd mobilization in SP-spiked soils. This inhibition could be a result of the suppression of SP dissolution, e.g., the formation of Cd–Ca mineralized layers[9] or the immobilization of released Cd species, which are in accord with the occurrence of precipitated Cd-bearing minerals (see below).

3.3 Cd mobilization at different Ca/S ratios in SP-spiked soils

Cd mobilization from SPs in soil environments is controlled by the dissolution rate of sphalerite and the coprecipitation of Cd with minerals such as calcite. According to our study, 5.22% (SP1 acidic), 1.36% (SP2 acidic), 6.90% (SP3 acidic), 6.12% (SP1 alkaline), 1.56% (SP2 alkaline), and 7.65% (SP3 alkaline) of EDTA-Cd and 0.41% (SP1 acidic), 0.09% (SP2 acidic), 0.80% (SP3 acidic) and 0.38 ‰ (SP1 alkaline), 0.47‰ (SP2 alkaline), and 0.22‰ (SP3 alkaline) of $CaCl_2$–Cd is annually released (Fig. S8). The annual net release of Cd is circa 0.35 (SP1), 1.19 (SP2), and 1.89 (SP3) μg per gram for carbonate-hosted SP in the acidic soils and 0.43 (SP1), 1.36 (SP2), and 2.10 (SP3) μg in the alkaline soils (Table S4), suggesting an indispensable accumulation of Cd in SP-spiked soils.

Our predicted values (Table S4) are lower than the previously observed values for ZnS spiked acidic soils (pH of 6.58) with ca. 114 μg Cd ZnS per g per a.[27] This indicates greater inhibition of Cd release from carbonate-hosted SP than from sphalerite alone. In this study, EPMA and SEM-EDS indicate that Cd occurs primarily in sphalerite and only slightly (ca. 1 wt%) in calcite and smithsonite (Fig. S2a). Similar Cd concentrations in secondary phases before (calcite) and after one year of incubation (clay-absorbed calcite) (Fig. S2b) also indicate that Cd mobility changes occur mainly in and around sphalerite particles.

3.4 Distribution of Cd in SP-spiked soils at the micrometer-to nanometer-scale

As similar percentages of Cd mobilization calculated by EDTA-extractable Cd occur in SP-spiked acidic and alkaline soils, an indispensable characterization for Cd species in soil constituents at the micrometer to nanometer scale is necessary to understand the mobility of Cd in both acidic and alkaline soil environments.

SP2-spiked acidic and alkaline soils with medium Ca/S ratios contain the highest Cd concentration and are selected for SEM analyses. The sample from the acidic soils contains highly weathered sphalerite grains, depicting etch pits and infillings of Al-silicates, Fe-(hydr)oxides and Zn-oxides (Fig. 1a, b, 2a and b). The dissolution of sphalerite and the formation of secondary Zn- and Cd-bearing minerals can be explored through nano-mineralogical characterization of the interface between sphalerite and secondary phases. Hence, two FIB lamellae were extracted along the interface of a sphalerite grain and infillings containing $CaCO_3$, Fe-(hydr)oxides and Zn-oxides (Fig. 1a and 2a). The extracted FIB lamellae depict high porosities along the interface of the sphalerite toward secondary phases (Fig. 1c and 2c).

In FIB lamella-1 (acidic soil), $CaCO_3$ coatings occur on Cd-bearing sphalerite with Zn/Cd mass ratios ranging from 26 : 1 to 82 : 1 (average of 50 : 1) (Fig. 1c–e). In sphalerite particles, ZnS inclusions occur, which are enriched in Ca and Pb. These inclusions depict wurtzite structure-type and form curved contact interfaces towards their cubic hosts (Fig. 1d–j). EDS-line scans across sphalerite–calcite interfaces indicate higher Zn/Cd than Ca/Cd ratios (CPS/CPS) (Fig. 1h), suggesting that Cd is enriched in calcite relative to sphalerite. The replacement of ZnS by $CaCO_3$, which leads to Cd enrichment in the $CaCO_3$ phase relative to ZnS, may reflect a thermodynamic preference analogous to the calcite–smithsonite system. In such systems, the lower solubility product of smithsonite ($ZnCO_3$; log $K_{sp} \approx$ −10.6) compared to calcite (log $K_{sp} \approx$ −8.3) drives Zn retention in the solid phase under equilibrium conditions. Similarly, $CdCO_3$ (log $K_{sp} \approx$ −12.3) likely exhibits even lower solubility than $ZnCO_3$, which favors Cd incorporation into calcite during interfacial dissolution–reprecipitation reactions.[35]

The occurrence of Cd–Pb-enriched wurtzite inclusions in cubic sphalerite indicates that the transformation of sphalerite to wurtzite (Fig. 1g) is based on a coupled dissolution–reprecipitation (CDR).[14] The formation of wurtzite inclusions via CDR and the replacement of sphalerite by calcite most likely contributed to the release of Cd. The interfacial porosity observed (Fig. 1f) between Cd-bearing ZnS and $CaCO_3$ likely facilitated the required fluid infiltration for the CDR and the formation of Cd–Pb-rich wurtzite nano-inclusions.

The formation of the Cd–Pb-rich wurtzite nano-inclusions and Cd-rich calcite may have occurred via the following steps: (I) oxidative dissolution of sphalerite and release of Zn^{2+}, Cd^{2+} and S^{2-} species by interfacial solutions enriched in Ca^{2+} and CO_3^{2-} due to the dissolution of the associated calcite; (II) precipitation of Cd-depleted ZnS before the formation of the Cd–Pb-wurtzite nano-inclusions due to the lower
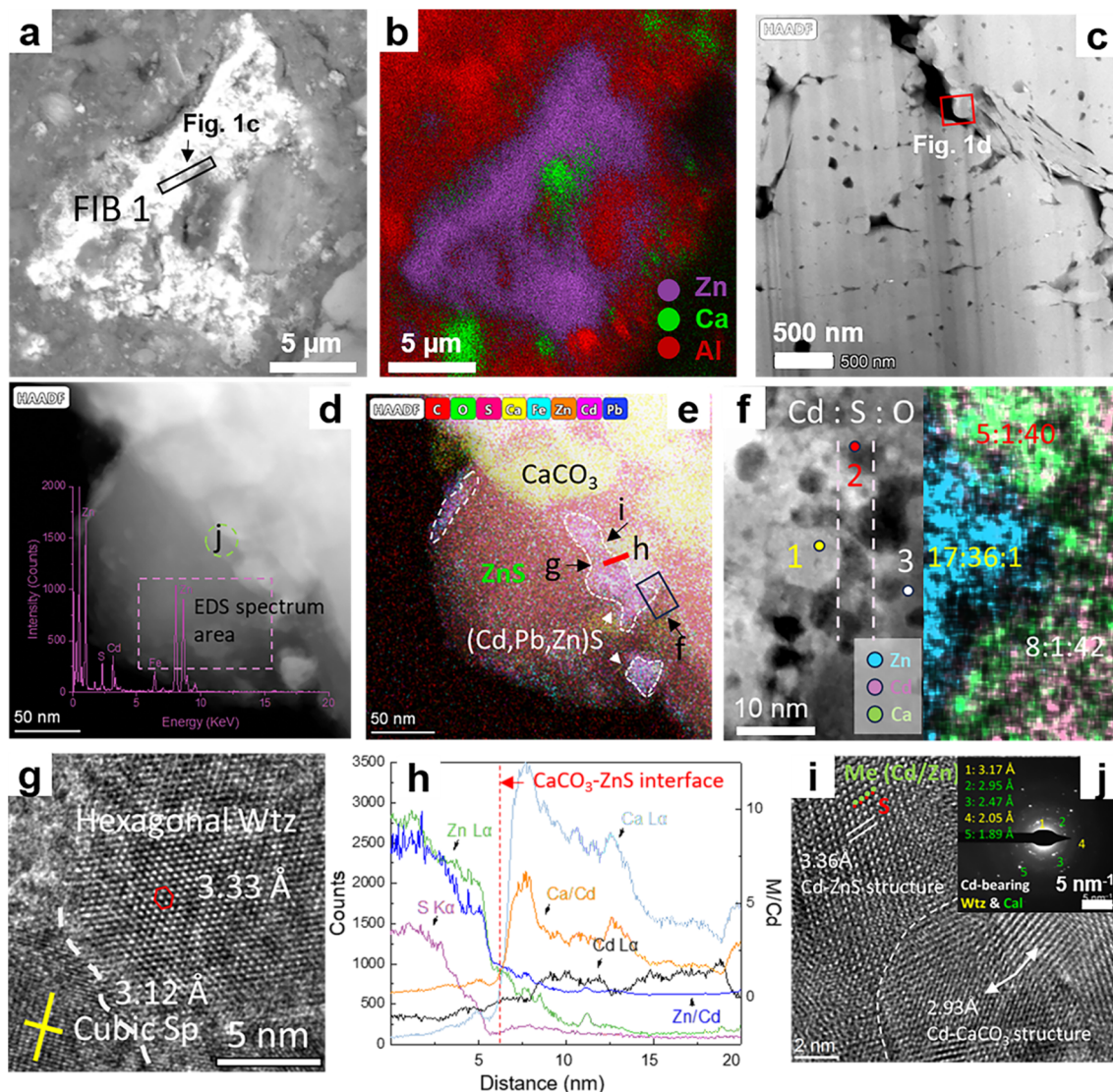
Fig. 1 SEM and TEM images of Zn-bearing grains in the SP2-spiked acidic soil. (a and b) SEM-EDS image and map indicating sphalerite–calcite interactions in soils; (c) FIB lamella; (d and e) TEM image and STEM-EDS map for a CaCO$_3$ and (Cd, Pb, Zn)S association on sphalerite; (f) STEM image and STEM map for a highly porous ZnS–CaCO$_3$ interface; (g) HRTEM image of an interface between cubic sphalerite and hexagonal wurtzite; (h) STEM-EDS line scans depicting higher Zn/Cd in sphalerite than Ca/Cd ratios in calcite (cps/cps) suggesting depletion and enrichment of Cd in ZnS and CaCO$_3$; (i and j) HRTEM and SAED images of the interface between Cd-bearing ZnS and Cd-bearing CaCO$_3$ structures. Wtz, wurtzite; Sp, sphalerite.

electrochemical potential[36] and solubility product of ZnS than that of CdS under an oxidative acidic soil environment;[37] (III) increasing saturation of the interfacial solution towards Cd-enriched calcite and Cd–Pb–Zn–S nano-inclusions, with the latter precipitating along the interface of Cd-depleted and enriched sphalerite and calcite, respectively. Similar processes were observed during the alteration of Cd-sphalerite under hydrothermal conditions, where CdS and PbS nano-inclusions formed within alteration layers of sphalerite.[13,35] The formation of nanomaterials during CDR in this and the latter studies is a common process in the critical zone and hydrothermal environments and has been observed in many other mineral systems.[15]

In FIB lamella-2 (alkaline soil), a goethite–sphalerite–zincite/hematite association occurs from the lower to the upper part of the lamella. Unlike the samples from the acidic soils, zincite (ZnO) is the major weathering product of sphalerite (Fig. 2d). HRTEM observations further indicate a common interface between Cd–Zn-bearing carbonate minerals, zincite and sphalerite, suggesting an interfacial CDR process in which the latter is replaced by the former two minerals (Fig. 2d–g). The stability of zincite under alkaline conditions arises from Zn^{2+} hydrolysis, which favors the dehydration of transient Zn-hydroxides (e.g., Zn(OH)$_2$) to ZnO at high pH, coupled with a low solubility of ZnO under alkaline conditions (log $K_s \approx$ 11–12). Zincite crystallizes in the wurtzite-structure type, with Zn being tetrahedrally coordinated. Due to the smaller ionic radius of O^{2-} versus S^{2-}, the
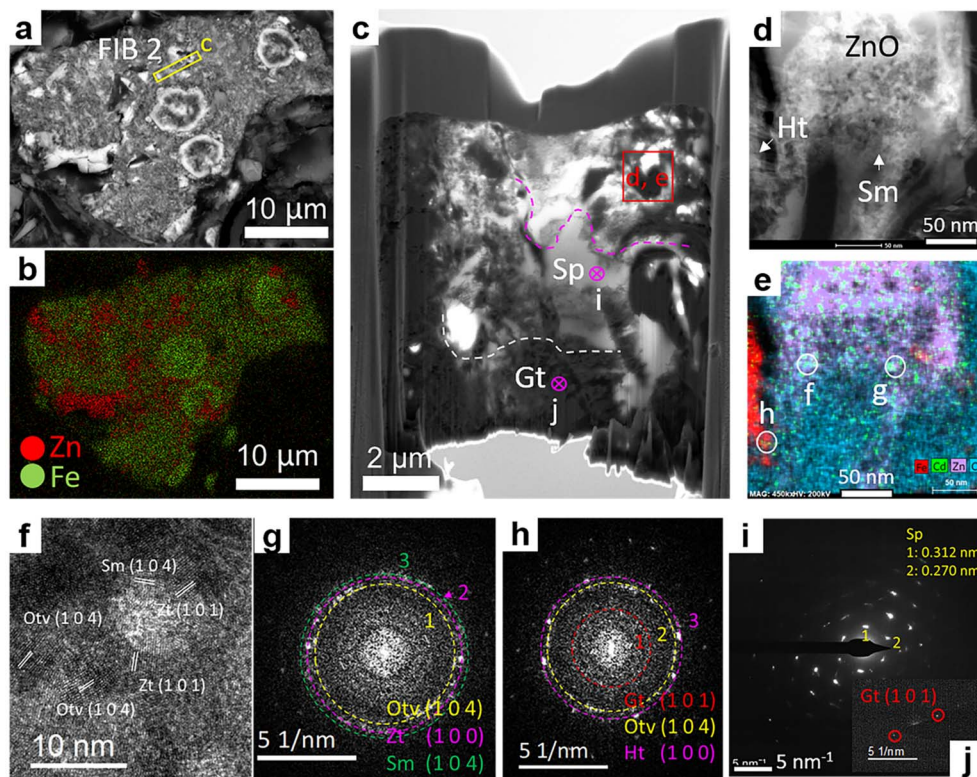
Fig. 2 SEM and TEM images of Zn-bearing grains in the SP2-spiked alkaline soil. (a and b) SEM-EDS images indicating complex mineral assemblages of Zn- and Fe-bearing phases; (c) FIB lamella 2 of goethite (Gt)-sphalerite (Sp)-zincite (Zt)/hematite (Ht) interfaces. (d–f) STEM image, STEM-EDS map and HR-TEM image of Cd-bearing smithsonite heterogeneously distributed on zincite and hematite; (g) and (h) FFT pattern for the latter assemblages; (i and j) SAED pattern of sphalerite and goethite in the lower part of the FIB lamella.

tetrahedral site can only incorporate a limited amount of the larger Cd (ionic radius for tetrahedrally coordinated Cd^{2+}: 0.92 Å vs. Zn^{2+}: 0.74 Å).[38] Additionally, the higher electronegativity of Cd versus Zn leads to a limited substitution of Zn by Cd in ZnO, as the stronger electronegativity of Cd makes it less likely to fit into the lattice structure of ZnO, where the oxygen (O) in ZnO is also highly electronegative, preferring to bond with the more electropositive Zn rather than Cd.[39,40] In addition, CdO is thermodynamically less favorable than $CdCO_3$ under alkaline conditions and thus leads to a kinetic barrier to CdO formation in alkaline soils.[41] As Cd^{2+} shows a higher structural compatibility with smithsonite, $ZnCO_3$, than zincite, Cd^{2+} released during the replacement of sphalerite by ZnO under alkaline conditions accumulates in smithsonite nano-inclusions (Fig. 2).

Under alkaline conditions, the formation of hematite over goethite is favored due to its lower solubility and higher stability at high pH.[42] However, the stability of Fe-(hydr)oxides is size-dependent with goethite being more stable than hematite at particle sizes in the nanometer-size range.[43,44] This may explain the occurrence of nano-sized goethite along cracks and pores (Fig. 2j) and the presence of a polyphase containing hematite and nano-sized goethite (Fig. 2h).

3.5 Nanometric distribution of Cd in colloids in soil solution

The nanoscale distribution and speciation of Cd in soil colloids are crucial to understanding its mobility, as colloidal interfaces

govern the partitioning of metals between dissolved and particulate phases. In this study, the unintermittent oxygen–water interface may highlight the formation and transformation of Cd-bearing colloids. Therefore, we further investigated the distribution and mineralogy of Cd-bearing colloids in the soil solution to evaluate how Ca/S ratios of sphalerite ore influence the mobility of Cd in the soil column.

The observed increases in Cd concentrations in the colloidal and truly dissolved fractions of the soil solution (<0.45 μm) during the incubation period confirm the ongoing dissolution of the SP ores. Here, the Cd concentrations in both fractions increase by ca. 100 times from day 0 to day 365, whereas the corresponding increases in the fractions extracted from the alkaline soils were not statistically significant (Fig. S9a and c). This is in contrast with the EDTA-extractable data (Fig. S7) and suggests a low contribution of the colloidal fractions (directly related to the water-soluble species) towards Cd mobility in alkaline soils. Therefore, we only extracted colloids from acidic soils for further TEM characterizations.

The proportions of Cd in the colloidal fractions range from 11% to 34% in all treatments (Fig. S9b and d). The highest and lowest concentrations of Cd in the colloidal fractions occur in the acidic and alkaline soils at days 365 and 0, respectively. At the initial stage (day 0), dispersive regular-shaped ZnS NPs are the dominant colloids in the leachates (Fig. 3a), reflecting the occurrence of unaltered SPs. With ongoing incubation, the proportion of Cd in the colloidal fractions increases, reaching

3658 | Environ. Sci.: Processes Impacts, 2025, 27, 3652–3664

This journal is © The Royal Society of Chemistry 2025

a maximum of 20% in the SP1-spiked acidic soil. The most common colloids at day 180 are aggregates of $ZnCO_3$- and ZnS-NPs with Zn/S atomic ratios of >1 (Fig. 3c and d). At day 365, aggregates containing Zn-, Cd-, and Fe-bearing NPs are the most common Zn-bearing colloids (Fig. 3e and f). Here, Cd–Zn- or Cd–Fe-bearing NPs are often associated closely (Fig. 3 and 4) with Cd-bearing $ZnCO_3$ NPs occasionally attached to Fe_2O_3 NPs. (Fig. 4b–f).

The proportions of Cd in the colloidal fractions of the leachates show a significant positive ($p < 0.05$) correlation with those of Fe and OM (Fig. S10), in accord with the TEM observations (Fig. 4a–c). In this study, the unintermittent oxygen–water interface provides conditions for Fe-colloid transformation. Soils under the interface are replete with microsites that undergo dynamic anoxia in response to high labile C loads during periods of high moisture and experience Fe^{III} reduction (Fig. S3). With a declining water table, the re-oxidized Fe^{III} hydrolyzes to ferrihydrite, transforming over time into hematite. During the latter process, Cd adsorbs or is structurally incorporated into hematite.[45,46] Above the oxygen–water interface, dissolved organic ligands can complex Fe^{III}, inhibiting particle growth by capping nascent nuclei and limiting the size of Fe_2O_3 NPs to tens of nanometers (Fig. 4).

The buffering of pH through CaCO3 dissolution leads to an increase in pH during incubation, promoting the adsorption of Cd to OM, which in turn facilitates OM aggregation (Fig. 4). Furthermore, the adsorption of low-molecular-weight organic acids (LMWOA) to Fe oxide surfaces promotes the complexation of Fe by LMWOA, which act as "bridges", binding Cd-bearing colloids into larger aggregates and occlusions within Fe-OM associations.[25]

The occurrence of adsorbed or structurally incorporated Zn- and Cd-species in hematite (Fig. 3 and 4) can be interpreted by a combination of geochemical processes, localized microenvironments, and interactions between Fe_2O_3, CO_3^{2-} and metals (Zn, Cd and Fe). Carbonate release by calcite dissolution promotes the formation of surface-bound $ZnCO_3$, $CdCO_3$ and $FeCO_3$ nuclei in microenvironments of near-neutral pH. The heterogeneous distribution of C with Fe further suggests a possible association between Fe-carbonates and hematite (Fig. 4c). $FeCO_3$ is less stable than $ZnCO_3/CdCO_3$ in fluctuating redox systems (even though the Eh is always larger than 150 mV) due to the potential oxidation of Fe^{2+}. The occurrence of lattice fringes corresponding to the siderite–calcite structure type in between domains of the otavite ($CdCO_3$)–calcite structure type and hematite indicates the presence of various carbonate structure-types with different abilities to sequester Cd (Fig. 4g). The identical orientation of lattice fringes of attached Cd-bearing $ZnCO_3$ domains (Fig. 4f) implies that these domains nucleate, grow and form crystalline aggregates.[47,48]

The formation of carbonate nanometer-sized domains on hematite in the colloidal fraction was promoted by (a) the high ionic strength of the soil solution; (b) the higher ratio of calcite *versus* sphalerite; (c) the continuous dissolution of calcite and the release of high concentrations of Ca and CO_3^{2-} (ref. 37)(Fig. 4); (d) the formation of carbonate coatings which may shield $ZnCO_3/CdCO_3$ from dissolution in acidic bulk soil and (e) the alteration of hematite by carbonate-rich solutions. This interplay highlights the significance of micro-scale geochemistry in controlling metal behavior, even in seemingly inhospitable (acidic) bulk environments.
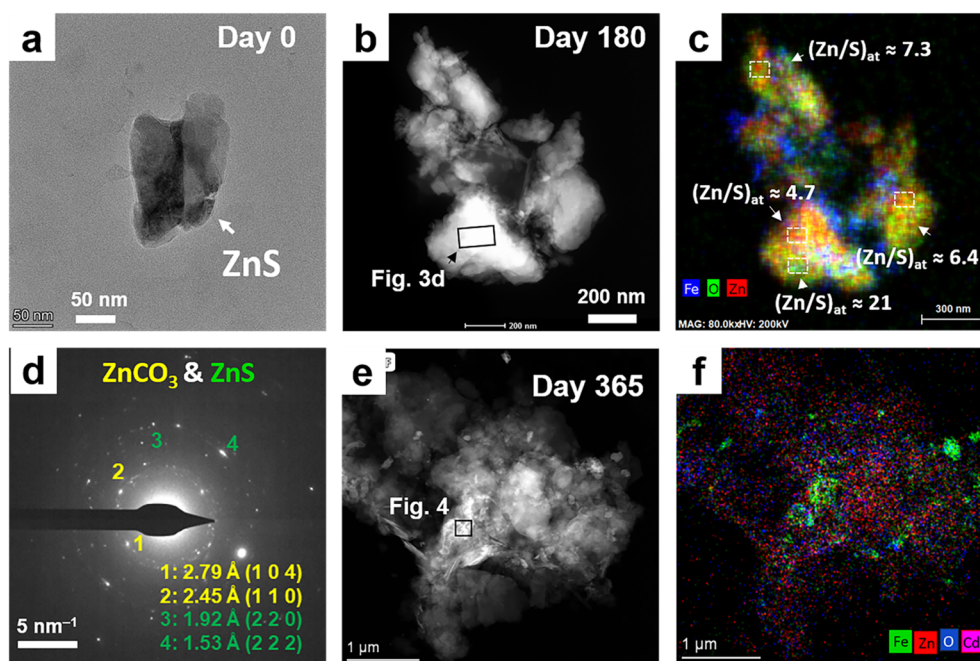

Fig. 3 TEM images of the colloids extracted from the SP2-spiked acidic soil. (a) ZnS NPs observed at day 0; (b–d) STEM image, STEM-EDS map and SAED pattern of a colloid composed of Zn-carbonates and Zn-sulfides at day 180; (e and f) TEM images and STEM-EDS map of a Cd–Zn-bearing colloid at day 365.

This journal is © The Royal Society of Chemistry 2025

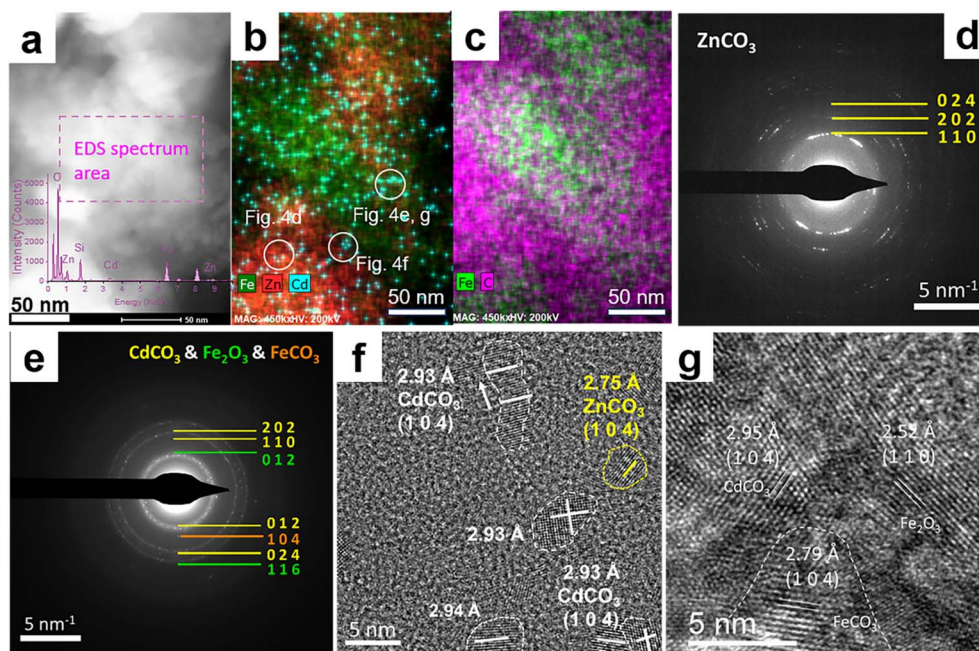*Environ. Sci.: Processes Impacts*, 2025, **27**, 3652–3664 | **3659**

Fig. 4 Higher resolution images for the area depicted in Fig. 3e. (a–c) STEM image, STEM-EDS maps indicate the co-distribution of Cd-bearing Fe- and Zn-phases embedded in OM; (d and e) SAED pattern; (f) and (g) HR-TEM-SAED images of Zn/Fe/CdCO$_3$ and Fe$_2$O$_3$ phases encircled in Fig. 4b.

4. Environmental implications

4.1 Quantification of Cd release mechanisms during SP ore weathering in soils

Changes in the APM to OPM ratios reflect the proton-buffering capacity of the soils and may be a helpful indicator for evaluating the quantitative contributions of different weathering mechanisms of metal sulfide minerals.[5,49] They are generally considered the main processes that explain the weathering of metal sulfides in the natural environment. Our study deciphered the impact of different Ca/S ratios on the weathering of carbonate-hosted SPs and Cd mobilization in soils.

The increase in EDTA-Cd with incubation time indicates continuous SP dissolution and Cd release into the soil (Fig. S7). OPM can mainly explain the SP dissolution and Cd release in alkaline soils due to the scarcity of H$^+$. For the acidic soils, up to 53% and 78% of OPM and APM contributed to the dissolution of SP, with their relative contribution declining as the Ca/S ratio decreased (Fig. S11). This suggests that calcite-rich environments in weak acidic soils are beneficial for sulfur-oxidizing dissolution of metal sulfides, as CaCO$_3$ in soils can create a more supportive environment for sulfur-oxidizing bacteria by managing pH levels, providing essential Ca^{2+} and possibly offering a carbon source.[50–52]

The dramatic increase in APM percentage from day 30 to day 90 in the SP1-spiked acidic soil suggests a possible tipping point, where an increase in the Ca/S ratio from SP1 to SP2 results in an exponential decrease in sulfide oxidation. The gradual increase in APM with the duration of the incubation suggests that the H$^+$ supplement by OPM surpasses the H$^+$ consumption by APM. Furthermore, $\Delta[\text{Cd}]_{\text{EDTA}}$ showed

a significant positive correlation (Table S6) with the ΔSO_4^{2-} (acidic soil, $r = 0.927$, $p < 0.01$; alkaline soil, $r = 0.906$, $p < 0.01$) and suggests that OPM contributed to the mobilization of Cd throughout the annual incubation.

The relationship between temporal changes in acid-promoting dissolution (APM) and oxidation-promoting dissolution (OPM) in bulk soils spiked with SP ores of different Ca/S ratios can be utilized for evaluating the mass balance between acid-producing sulfide oxidation and acid-consuming carbonate dissolution in soils and tailings hosting residuals of carbonate-hosted base-metal ores. The temporal APM-OPM relationships quantify the carbonate buffering capacity in tailings. For instance, a declining Ca/S ratio over incubation time signals the eventual exhaustion of carbonate, heralding the generation of acid mine drainage (AMD) and sustained Cd release. Climate warming may accelerate sulfide oxidation rates,[53] thereby shortening the timescale for the decline in calcite/sulfide ratio in soils around Zn deposits. This could exacerbate Cd release in temperate regions experiencing increased rainfall (enhanced leaching) in the form of colloidal species like Cd-bearing smithsonite (Fig. 4). By quantifying the APM-OPM interplay with different Ca/S ratios in sulfide-impacted soils, our findings help bridge the gap between theoretical geochemistry and real-world environmental management.

4.2 Implications for soil remediation in carbonate-rich soils

Our study also broadens the insight into elucidating the mobility of Cd in sphalerite ores with varying Ca/S ratios through nanoscale pore structures and chemical gradient

3660 | *Environ. Sci.: Processes Impacts*, 2025, **27**, 3652–3664

This journal is © The Royal Society of Chemistry 2025

distributions. Electron microscopy indicates that $CaCO_3$ induces a spatial gradient of Cd species shifting from Cd-depleted ZnS to Cd-rich $CaCO_3$, the precipitation with (Cd, Ca)CO_3 NPs at sphalerite–calcite interfaces (Fig. 1), and the mobilization of Cd via Ca- and Cd-rich organic colloids in acidic soils (Fig. 3). Under alkaline conditions, ZnO is the most stable Zn phase, and the incompatibility of Cd^{2+} with its structure favors the formation of Cd-bearing smithsonite (Fig. 2). The preferential sequestration of Cd into carbonates rather than oxides reflects its stronger affinity for carbonate ligands under alkaline conditions and kinetic barriers to CdO formation, which is less thermodynamically favored than otavite ($CdCO_3$) in carbonate-rich systems. Hence, the divergence of Zn and Cd with respect to structural compatibility, ligand availability, and solubility affects their partitioning during the weathering of carbonate-hosted sphalerite. As carbonates are more vulnerable to acidity than oxides, Cd sequestered under alkaline conditions by smithsonite precipitates may be remobilized during pH perturbations towards lower pH values (e.g., acid rain or organic acid exudates).

In addition to these mineralogical processes, our results highlight the important role of colloids in controlling Cd mobility. Significant positive correlations (Fig. S10) between Cd, Fe, and OM in the colloidal fraction, supported by TEM observations of Cd-bearing carbonate NPs embedded within Fe–OM aggregates, suggest that Cd is efficiently stabilized in colloidal form. Such Fe–OM–Cd colloids could remain suspended in soil porewaters and migrate over considerable distances. Under fluctuating redox and pH conditions, these colloids may re-disperse or aggregate, representing an overlooked but potentially dominant pathway for Cd transport in carbonate-rich soils. This is particularly relevant for karst regions, where abundant Ca can promote flocculation and re-dispersion cycles of the aforementioned ternary colloid, increasing the chances of Cd transport into groundwater or surface water.[54] Importantly, Cd that is initially retained in secondary phases such as carbonate species or Ca-rich Fe-OM colloids may later undergo secondary mobilization in acidic soils and under redox fluctuating conditions.[55] Hence, our studies show that risks of Cd contamination in karst soils may not be limited to the initial release of Cd from PM (e.g., sphalerite) but may also arise from the cycling of Cd between pore solutions, colloidal fractions and secondary minerals.

Although a limited number of soil types and sphalerite ores were used in this study, this design allowed us to understand the main controls on Cd mobilization in carbonate-rich soils. The Zn ores cover a range of carbonate alteration levels, while the two soils represented acidic and alkaline environments. This framework revealed several important nanoscale Cd pathways, including release from PM, colloid formation, and secondary carbonate precipitation. These findings likely represent the most common processes in actual environments and could be applicable to soil management and risk assessment in mining-affected karst regions. To support remediation efforts in carbonate-rich Cd-contaminated soils, future studies should focus on (a) validating the observed nanoscale mechanisms in more complex environments, particularly in light of climate change; (b) incorporation of the observed secondary phases into predictive models and (c) quantification of the colloidal fraction using state-of-the-art single particle ICP-MS.[56]

5. Conclusions

This study reveals that carbonate-hosted sphalerite weathering controls Cd mobilization through both bulk geochemical processes and nanoscale pathways. Bulk analyses indicated that Cd mobilization rates were 0.35–2.10 μg per g SP per year, with higher Ca/S ratios of carbonate-hosted SP significantly inhibiting Cd release. In acidic soils, both acid-promoting (APM) and oxidation-promoting (OPM) processes drove sphalerite dissolution, but APM became dominant as carbonate buffering declined. This demonstrates that the carbonate content regulates the balance between acid generation and neutralization, influencing the potential for Cd release. Microscopic analyses further revealed different retention pathways in acidic and alkaline soils. In acidic soils, Cd was released from sulfides and sequestered by secondary carbonate phases through interfacial dissolution–precipitation. In alkaline soils, Cd was not sequestered by ZnO due to structural incompatibility, but instead formed Cd-bearing carbonates bound to Fe (hydr) oxides. The presence of Cd-bearing carbonates and Cd–Fe-organic colloids in soil solutions suggests that Cd is often structurally incorporated into colloids and that these are the primary carriers of Cd in carbonate-rich systems. These observed nanoscale processes underscore that bulk data alone cannot capture the fate of Cd in soil environments, highlighting the mineralogical and geochemical complexity that controls Cd behavior during carbonate-hosted sphalerite dissolution in various soil environments.

Author contributions

X. L. designed the methodology, conducted the investigation, curated and analyzed the data, and wrote the original draft. J. L. contributed to the investigation and draft edits. P. H., J. Z., Y. L., and M. S. reviewed and edited the manuscript. L. W. administered the project and acquired funding.

Conflicts of interest

There are no conflicts to declare.

Data availability

The data supporting this article have been included as part of the supplementary information (SI). Supplementary information: additional experimental details for materials and methods, along with supplementary figures and tables for this article. Method of soil physicochemical analysis; method of mineralogical analysis of SP ores by XRD; details of soil incubations and leaching experiments; method of total and extractable Cd and Zn determination; Table S1 shows basic physicochemical properties of the testing soil; Table S2 shows elemental distribution in testing SP ores; Table S3 presents

This journal is © The Royal Society of Chemistry 2025

Environ. Sci.: Processes Impacts, 2025, **27**, 3652–3664 | **3661**

Pearson correlation coefficients among ΔCd, ΔSO_4^{2-}, ΔpH, and Ca/S ratio in SP-spiked soils; Table S4 reports the net Cd release after 30 to 365 days of incubation; Table S5 details elemental distribution and pH in SP-spiked soils on day 0; Table S6 provides parameters for calculating APM and OPM; Fig. S1 illustrates the mineral composition of three Zn ores; Fig. S2 shows Cd-bearing Zn minerals in sphalerite analyzed by EPMA and EDS; Fig. S3 depicts redox potential and Fe^{2+} dynamics during soil incubation; Fig. S4 demonstrates soil pH, CO_3^{2-} decreasing, and SO_4^{2-} increasing in SP-spiked soils over incubation time; Fig. S5 shows the temporal change of soil pH; Fig. S6 presents correlations between soil pH and sulfate changes over time in SP-spiked acidic soil; Fig. S7 shows concentrations of mobilized Cd calculated by $CaCl_2$- and EDTA-Cd in SP-spiked soils; Fig. S8 indicates Cd mobilization rates in acidic and alkaline soils with different Zn ore spiking; Fig. S9 details concentrations and percentages of mobilized Cd in truly dissolved and nanoparticulate fractions in soil leachates; Fig. S10 shows the linear correlation between nanoparticulate Cd and nanoparticulate Fe and OM in the acidic soil; Fig. S11 presents the contribution rates of OPM and APM in the acidic soil. See DOI: **https://doi.org/10.1039/d5em00405e**.

Acknowledgements

References

1 T. Wu, Z. Huang, Y. He, M. Yang, H. Fan, C. Wei, L. Ye, Y. Hu, Z. Xiang and C. Lai, Metal source and ore-forming process of the Maoping carbonate-hosted Pb-Zn deposit in Yunnan, SW China: Evidence from deposit geology and sphalerite Pb-Zn-Cd isotopes, *Ore Geol. Rev.*, 2021, **135**, 104214.

2 Z. Bao, T. Al, J. Bain, H. K. Shrimpton, Y. Z. Finfrock, C. J. Ptacek and D. W. Blowes, Sphalerite weathering and controls on Zn and Cd migration in mine waste rock: An integrated study from the molecular scale to the field scale, *Geochim. Cosmochim. Acta*, 2022, **318**, 1–18.

3 A. Bufe, N. Hovius, R. Emberson, J. K. Rugenstein, A. Galy, H. J. Hassenruck-Gudipati and J. M. Chang, Co-variation of silicate, carbonate and sulfide weathering drives CO_2 release with erosion, *Nat. Geosci.*, 2021, **14**(4), 211–216.

4 Y. Kanzaki, S. L. Brantley and L. R. Kump, A numerical examination of the effect of sulfide dissolution on silicate weathering, *Earth Planet. Sci. Lett.*, 2020, **539**, 116239.

5 M. Valencia-Avellan, R. Slack, A. Stockdale and R. J. G. Mortimer, Understanding the mobilisation of metal pollution associated with historical mining in a carboniferous upland catchment, *Environ. Sci. Proc. Imp.*, 2017, **19**(8), 1061–1074.

6 S. Paradis, H. Keevil, G. J. Simandl and M. Raudsepp, Carbonate-hosted nonsulphide Zn–Pb mineralization of southern British Columbia, Canada, *Miner. Deposita*, 2015, **50**(8), 923–951.

7 N. Mondillo, M. Boni, G. Balassone and I. M. Villa, The Yanque prospect (Peru): From polymetallic Zn-Pb mineralization to a nonsulfide deposit, *Econ. Geol.*, 2014, **109**(6), 1735–1762.

8 X. Li, J. Zhou, P. Hu, T. Zhou, Z. Li, Y. Luo, L. Wu and M. Schindler, Colloids control the mobilization of released zinc-and cadmium-species in calcite-rich soils, *Geochim. Cosmochim. Acta*, 2024, **387**, 12–27.

9 T. Yin, H. Lin, Y. Dong, Z. Wei, B. Li, C. Liu and X. Chen, Inhibition of cadmium releasing from sulfide tailings into the environment by carbonate-mineralized bacteria, *J. Hazard. Mater.*, 2021, **419**, 126479.

10 P. Cubillas, S. Köhler, M. Prieto, C. Causserand and E. H. Oelkers, How do mineral coatings affect dissolution rates? An experimental study of coupled $CaCO_3$ dissolution—$CdCO_3$ precipitation, *Geochim. Cosmochim. Acta*, 2005, **69**(23), 5459–5476.

11 X. Zhang, J. Guo, S. Wu, F. Chen and Y. Yang, Divalent heavy metals and uranyl cations incorporated in calcite change its dissolution process, *Sci. Rep.*, 2020, **10**(1), 16864.

12 J. J. Kim, S. S. Lee, P. Fenter, S. C. Myneni, V. Nikitin and C. A. Peters, Carbonate Coprecipitation for Cd and Zn Treatment and Evaluation of Heavy Metal Stability Under Acidic Conditions, *Environ. Sci. Technol.*, 2023, **57**(8), 3104–3113.

13 Y. Kim, A. Tekawade, S. S. Lee and P. Fenter, Morphological and crystallographic controls in the replacement of calcite and aragonite by cerussite and otavite, *Geochim. Cosmochim. Acta*, 2023, **341**, 16–27.

14 H. Duan, C. Wang, R. Hu, J. Zhu and J. Deng, Supernormal enrichment of cadmium in sphalerite via coupled dissolution-reprecipitation process, *Commun. Earth Environ.*, 2023, **4**(1), 356.

15 M. Schindler, J. Xu and M. F. Hochella Jr, Abiotic and biotic-controlled nanomaterial formation pathways within the Earth's nanomaterial cycle, *Commun. Earth Environ.*, 2024, **5**(1), 646.

16 L. Liu and C. Lin, A calcite → aragonite-type phase transition in $CdCO_3$, *Am. Mineral.*, 1997, **82**(5–6), 643–646.

17 C. V. Reddy, J. Shim and M. Cho, Synthesis, structural, optical and photocatalytic properties of CdS/ZnS core/shell nanoparticles, *J. Phys. Chem. Solids*, 2017, **103**, 209–217.

18 M. Sanakousar, V. CC, V. M. Jiménez-Pérez, B. Jayanna, A. Shridhar and K. Prakash, Efficient photocatalytic degradation of crystal violet dye and electrochemical performance of modified MWCNTs/Cd-ZnO nanoparticles with quantum chemical calculations, *J. Hazard. Mater. Adv.*, 2021, **2**, 100004.

19 S. B. Woodley, A. A. Sokol, C. R. A. Catlow, A. A. Al-Sunaidi and S. M. Woodley, Structural and Optical Properties of Mg and Cd Doped ZnO Nanoclusters, *J. Phys. Chem. C*, 2013, **117**(51), 27127–27145.

3662 | *Environ. Sci.: Processes Impacts*, 2025, **27**, 3652–3664

This journal is © The Royal Society of Chemistry 2025

20 G. T. Getahun, A. Etana, L. J. Munkholm and H. Kirchmann, Liming with CaCO$_3$ or CaO affects aggregate stability and dissolved reactive phosphorus in a heavy clay subsoil, *Soil Tillage Res.*, 2021, **214**, 105162.

21 A. Beauvois, D. Vantelon, J. Jestin, C. Rivard, M. Bouhnik-Le Coz, A. Dupont, V. Briois, T. Bizien, A. Sorrentino and B. Wu, How does calcium drive the structural organization of iron–organic matter aggregates? A multiscale investigation, *Environ. Sci. Nano*, 2020, **7**(9), 2833–2849.

22 A. Beauvois, D. Vantelon, J. Jestin, M. Bouhnik-Le Coz, C. Catrouillet, V. Briois, T. Bizien and M. Davranche, How crucial is the impact of calcium on the reactivity of iron–organic matter aggregates? Insights from arsenic, *J. Hazard. Mater.*, 2021, **404**, 124127.

23 X. Li, J. Zhou, T. Zhou, Z. Li, P. Hu, Y. Luo, P. Christie and L. Wu, Potential mobilization of cadmium and zinc in soils spiked with smithsonite and sphalerite under different water management regimes, *J. Environ. Manage.*, 2022, **324**, 116336.

24 X. Li, L. Wu, J. Zhou, Y. Luo, T. Zhou, Z. Li, P. Hu and P. Christie, Potential environmental risk of natural particulate cadmium and zinc in sphalerite-and smithsonite-spiked soils, *J. Hazard. Mater.*, 2022, **429**, 128313.

25 X. Li, Z. Cao, Y. Du, Y. Zhang, J. Wang, X. Ma, P. Hu, Y. Luo and L. Wu, Multi-metal contaminant mobilizations by natural colloids and nanoparticles in paddy soils during reduction and reoxidation, *J. Hazard. Mater.*, 2024, **461**, 132684.

26 L. C. Kon, S. Durucan and A. Korre, The development and application of a wind erosion model for the assessment of fugitive dust emissions from mine tailings dumps, *Int. J. Min. Reclam. Environ.*, 2007, **21**(3), 198–218.

27 T. Robson, C. Braungardt, J. Rieuwerts and P. Worsfold, Cadmium contamination of agricultural soils and crops resulting from sphalerite weathering, *Environ. Pollut.*, 2014, **184**, 283–289.

28 I. Blondet, E. Schreck, J. Viers, S. Casas, I. Jubany, N. Bahi, C. Zouiten, G. Dufrechou, R. Freydier and C. Galy-Lacaux, Atmospheric dust characterisation in the mining district of Cartagena-La Union, Spain: Air quality and health risks assessment, *Sci. Total Environ.*, 2019, **693**, 133496.

29 A. Navel, G. Uzu, L. Spadini, S. Sobanska and J. M. F. Martins, Combining microscopy with spectroscopic and chemical methods for tracing the origin of atmospheric fallouts from mining sites, *J. Hazard. Mater.*, 2015, **300**, 538–545.

30 L. Chen, J. Wang, W. Wei, B. Fu and D. Wu, Effects of landscape restoration on soil water storage and water use in the Loess Plateau Region, China, *For. Ecol. Manage.*, 2010, **259**(7), 1291–1298.

31 S. He, T. Liu, C. Kang, H. Xue, S. Sun and S. Yu, Photodegradation of dissolved organic matter of chicken manure: Property changes and effects on Zn^{2+}/Cu^{2+} binding property, *Chemosphere*, 2021, **276**, 130054.

32 K. T. Kim, G. Henkelman, L. E. Katz and C. J. Werth, New insights into calcite dissolution mechanisms under water, proton, or carbonic acid-dominated conditions, *Environ. Sci. Technol.*, 2024, **58**(26), 11331–11341.

33 M. Moncur, C. Ptacek, D. Blowes and J. Jambor, Release, transport and attenuation of metals from an old tailings impoundment, *Appl. Geochem.*, 2005, **20**(3), 639–659.

34 B. Xing, J. Mao, X. Xiao, H. Liu, C. Zhang, S. Guo, H. Li, W. Huang and C. Lai, Metallogenic discrimination by sphalerite trace element geochemistry: An example from the Fengyan Zn-Pb deposit in central Fujian, SE China, *Ore Geol. Rev.*, 2022, **141**, 104651.

35 C. Xu, P. Nong, Z. Zhu, Q. Kong, X. Zhou, H. Deng, S. Tang, L. Zhang and Y. Zhu, Dissolution and solubility of the solid solution between calcite and smithsonite [(Ca$_{1-x}$Zn$_x$) CO$_3$] at 25 °C, *ACS Earth Space Chem.*, 2023, **7**(7), 1401–1415.

36 H. Huang, H. Chen, P. M. Kopittke, R. Kretzschmar, F. Zhao and P. Wang, The voltaic effect as a novel mechanism controlling the remobilization of cadmium in paddy soils during drainage, *Environ. Sci. Technol.*, 2021, **55**(3), 1750–1758.

37 K. Barrett and M. B. McBride, Dissolution of zinc-cadmium sulfide solid solutions in aerated aqueous suspension, *Soil Sci. Soc. Am. J.*, 2007, **71**(2), 322–328.

38 L. L. George, N. J. Cook and C. L. Ciobanu, Partitioning of trace elements in co-crystallized sphalerite–galena–chalcopyrite hydrothermal ores, *Ore Geol. Rev.*, 2016, **77**, 97–116.

39 K. Yamamoto, T. Tsuboi, T. Ohashi, T. Tawara, H. Gotoh, A. Nakamura and J. Temmyo, Structural and optical properties of Zn (Mg, Cd) O alloy films grown by remote-plasma-enhanced MOCVD, *J. Cryst. Growth*, 2010, **312**(10), 1703–1708.

40 L. Pauling, The nature of the chemical bond—1992, *J. Chem. Educ.*, 1992, **69**(7), 519.

41 B. Asirvatham and Z. Munir, The decomposition of cadmium carbonate in air and in vacuum, *J. Mater. Sci.*, 1986, **21**, 1997–2001.

42 F. E. Furcas, B. Lothenbach, S. Mundra, C. N. Borca, C. C. Albert, O. B. Isgor, T. Huthwelker and U. M. Angst, Transformation of 2-line ferrihydrite to goethite at alkaline pH, *Environ. Sci. Technol.*, 2023, **57**(42), 16097–16108.

43 A. Navrotsky, L. Mazeina and J. Majzlan, Size-driven structural and thermodynamic complexity in iron oxides, *Science*, 2008, **319**(5870), 1635–1638.

44 A. Navrotsky, C. Ma, K. Lilova and N. Birkner, Nanophase transition metal oxides show large thermodynamically driven shifts in oxidation-reduction equilibria, *Science*, 2010, **330**(6001), 199–201.

45 C. Chen, S. J. Hall, E. Coward and A. Thompson, Iron-mediated organic matter decomposition in humid soils can counteract protection, *Nature Commun.*, 2020, **11**(1), 2255.

46 Q. Sun, E. D. Burton, Z. Yu, L. Chen, L. Bi, P. Cui and Y. Wang, Iron, sulfur, and carbon dynamics collectively regulate the fate of cadmium over the sulfidation-reoxidation cycle, *Environ. Sci. Technol.*, 2025, **59**(14), 7297–7309.

This journal is © The Royal Society of Chemistry 2025

Environ. Sci.: Processes Impacts, 2025, **27**, 3652–3664 | **3663**

47 G. Mirabello, A. Ianiro, P. H. Bomans, T. Yoda, A. Arakaki, H. Friedrich, G. de With and N. A. Sommerdijk, Crystallization by particle attachment is a colloidal assembly process, *Nat. Mater.*, 2020, **19**(4), 391–396.

48 V. Schoeppler, D. Stier, R. J. Best, C. Song, J. Turner, B. H. Savitzky, C. Ophus, M. A. Marcus, S. Zhao and K. Bustillo, Crystallization by amorphous particle attachment: on the evolution of texture, *Adv. Mater.*, 2021, **33**(37), 2101358.

49 S. M. Hayes, R. A. Root, N. Perdrial, R. M. Maier and J. Chorover, Surficial weathering of iron sulfide mine tailings under semi-arid climate, *Geochim. Cosmochim. Acta*, 2014, **141**, 240–257.

50 M. Al-Amri, Y. Souissi, D. Menezes-Blackburn, A. Al-Mayahi, S. Al-Ismaily, B. Al-Siyabi and V. Rethinasamy, Bacterial communities associated with the oxidation of elemental sulfur in calcareous soils of Oman, *J Soil Sci. Plant Nut.*, 2024, **24**, 1–14.

51 P. Gao and K. Fan, Sulfur-oxidizing bacteria (SOB) and sulfate-reducing bacteria (SRB) in oil reservoir and biological control of SRB: a review, *Arch. Microbiol.*, 2023, **205**(5), 162.

52 D. J. Leprich, B. E. Flood, P. R. Schroedl, E. Ricci, J. J. Marlow, P. R. Girguis and J. V. Bailey, Sulfur bacteria promote dissolution of authigenic carbonates at marine methane seeps, *ISME J.*, 2021, **15**(7), 2043–2056.

53 N. Jiao, T. Luo, Q. Chen, Z. Zhao, X. Xiao, J. Liu, Z. Jian, S. Xie, H. Thomas, G. J. Herndl and R. Benner, The microbial carbon pump and climate change, *Nat. Rev. Microbiol.*, 2024, **22**(7), 408–419.

54 M. C. Rowley, S. Grand and É. P. Verrecchia, Calcium-mediated stabilisation of soil organic carbon, *Biogeochemistry*, 2018, **137**(1), 27–49.

55 R. Wei, J. Liu, M. Li, W. Xie, J. Li, L. Liu, Y. Jiang, S. Sun, T. Deng, S. Wang and Y. Tang, Insights into toxic elements mobilization in Karstic paddy soil of southwest China: The overlooked significance of Iron-organic matter colloids, *Environ. Pollut.*, 2025, **383**, 126897.

56 H. Walch, N. Bašić, A. Praetorius, F. von der Kammer and T. A. Hofmann, versatile test system to determine nanomaterial heteroagglomeration attachment efficiency, *Environ. Sci.: Nano*, 2024, **11**(2), 588–600.

3664 | *Environ. Sci.: Processes Impacts*, 2025, **27**, 3652–3664

This journal is © The Royal Society of Chemistry 2025